Finite strain analysis of non-uniform deformations inside shear bands in sands

Olivier Chupin, Amy L Rechenmacher, Sara Abedi

Finite strain analysis of nonuniform deformation inside shear bands in sands

O. Chupin[1], A. L. Rechenmacher[2,*,†] and S. Abedi[2]

[1]*Université Nantes-Angers-Le Mans, Laboratoire Central des Ponts et Chausses, Nantes, France*
[2]*Civil and Environmental Engineering, University of Southern California, Los Angeles, California, USA*

A methodology has been developed to extend the incremental (Eulerian) Digital Image Correlation (DIC) technique to enable a Lagrangian-based large-strain analysis framework to examine the nature of strain and kinematic nonuniformity within shear bands in sands. Plane strain compression tests are performed on dense sands in an apparatus that promotes unconstrained persistent shear band formation. DIC is used to capture incremental, grain-scale displacements in and around shear bands. The performance of the developed accumulation algorithm is validated by comparing accumulated displacements with two sources of reference measurements. A comparison between large and infinitesimal rotation is performed, demonstrating the nature of straining within shear bands in sands and the necessity of using a finite strain formulation to characterize ensuing behavior. Volumetric strain variation along the shear band is analyzed throughout macroscopic postpeak deformation. During softening, volumetric activity within the shear band is purely dilative. During the global critical state, the shear band material is seen on the average to deform at zero volumetric strain; however, locally, the sand is seen to exhibit significant nonzero volumetric strain, putting into question the current definition of critical state. At the softening-critical state transition, a spatially periodic pattern of alternating contraction and dilation along the shear band is evidenced, and a preliminary evaluation indicates that the periodicity appears to be a physical phenomenon dictated only in part by median grain size.

KEY WORDS: shear band; sand; length scale; granular material; Digital Image Correlation (DIC); critical state

1. INTRODUCTION

The globally observed geomechanical response phenomena of postpeak softening and dilation in dense sands go hand-in-hand with shear band formation. In an elemental specimen, once a single persistent shear band has fully formed (in the absence of boundary interference), the shear band material is the only active material involved in significant deformation [1,2]. Recognizing then that the shear band material entirely controls global postpeak response, it is necessary to understand the underlying nature of granular material behavior within the shear band to fully and accurately characterize the softening and critical state material responses.

Numerous experimental and numerical research works have lead to a variety of discoveries about the underlying local micro-, and mesoscale processes within shear bands that govern postpeak response in sands. For instance, grain rotation has been found to play a significant role in manifesting shear band response (e.g. [3–6]). Several experimental works (e.g. [7–10]) have highlighted that the shear band material undergoes significantly higher volumetric dilation locally than that reflected

*Correspondence to: A.L. Rechenmacher, Civil and Environmental Engineering, University of Southern California, Los Angeles, California, USA.
†E-mail: arechenm@usc.edu

through global response. Similar results have been found numerically [6]. Oda and Kazama [11] found experimental evidence on the presence of large void spaces within shear bands, which were hypothesized to be formed from the buckling of column-like structures, or force chains, within the shear band [5]. Additional research has provided evidence of simultaneous local dilation and contraction occurring along shear bands during the critical state [5,10,12,13].

It is commonly accepted that the buckling of force chains forms the primary mesoscale mechanism leading to macroscopic softening within shear bands (e.g. [13–17]). In turn, recent attention has been drawn to the recognition that shear band deformation is largely nonaffine, and this nonaffinity arises not only from buckling force chains but also from microbands [16] and vortex structures [16,18,19]. Walsh *et al*. [20] demonstrate the importance of considering mesoscale particle-group interactions in generating realistic macroscopic granular response by including particle-group interactions; more realistic models of shear banding, strain softening, and dilation were obtained, i.e. considering that binary interactions between particles is not enough to produce realistic behavior. Further, the implementation and refinement of models that incorporate microscale or mesoscale rotations (e.g. higher gradient models) require an accurate characterization of the microscale and mesoscale kinematics occurring in the shear band. Thus, understanding the precise nature of these mesoscale kinematic features will play a key role in advancing understanding of the physical phenomena responsible for strain localization, softening, and macroscopic stress evolution in sands, as well as the understanding of jamming and flow in dense granular materials in general.

While the research findings mentioned above have considerably advanced our understanding of the underlying nature of shear band deformation, less attention has been paid to the possibility of a spatially patterned or systematic nature to the nonaffine kinematics observed within shear bands. The technique of Digital Image Correlation (DIC), which enables nondestructive local displacement evaluation through gray-level pixel mapping, has proven a valuable tool for experimental study of local displacement behavior in granular materials, such as sand. While DIC use in granular materials has largely focused on macroscopic shear band properties, such as thickness, inclination, and patterning (e.g. [21–23]), few recent works have focused on kinematic behavior internal to the shear band. Lesniewska and Wood [24] found "microbands" of alternating dilation and contraction, which seemed to evidence a regular spacing, along a macroscopic shear zone formed in glass beads. Rechenmacher [25] and Rechenmacher *et al*. [13] calculated various kinematic quantities along shear bands from DIC displacement fields in sands undergoing plane strain compression. Their results revealed a distinct seemingly spatial periodic pattern in the kinematics along the length of the shear band at the softening-critical state transition. This pattern was argued to mark a collective coordinated multiforce chain collapse event, offering one of the first glimpses of the evolution of active force chain activity in a real granular material.

In the work by Rechenmacher [25] described above, DIC analyses were performed at more than fairly large strain increments, which can compromise DIC precision. Chupin and Rechenmacher [26] and Rechenmacher *et al*. [13] circumvented this problem by utilizing a methodology developed to accumulate consecutive small-strain DIC analyses to derive large strain behavior. Here, we disclose the details of this methodology, to support both previous findings, as well as the findings presented here, which focus on the assessment of local volumetric strain evolution, spatial nonuniformity, and patterning within shear bands. Further, the accumulation of incremental DIC analyses has recently been accommodated in some commercial DIC codes that emphasize the interest and relevance of methods to handle this problem. Such a procedure holds tremendous promise toward the further study of mesoscale kinematics in shear bands, for example, this methodology has recently enabled the discovery that the kinematic patterns seen by Rechenmacher *et al*. [13] are related to the presence of vortex structures along the shear band [19]. The spatial periodicity in kinematic activity and the size, shape, spacing and evolution of associated vortices likely relate to an underlying length scale governing granular material deformation. The DIC method and our associated accumulation algorithm have the potential to play an important role in pursuing improved understanding of how such mesoscale deformational and kinematic processes control granular material behavior.

Herein, we describe in detail our methodology developed to accumulate incremental (Eulerian) DIC displacement data to enable Lagrangian-based large-strain analysis of local kinematics and strain associated with shear banding in dense sands. The resulting finite strain measures are then used to

evaluate volumetric strain nonuniformity and ensuing spatial and temporal patterning of volumetric strain variations, within shear bands in sands. The paper is organized as follows: We first describe the plane strain apparatus, testing methods, and DIC technique for quantifying local grain-scale displacements. We then describe the approach to accumulating incremental DIC results to obtain quantitative displacement behavior over finite strain increments. Lagrangian strain measures and kinematic quantities are then defined. The performance of the accumulation algorithm is validated by comparing accumulated displacements with two sources of reference measurements. The nature of shear band straining is exemplified through a comparison between large and infinitesimal rotation. Volumetric strain along the shear band is analyzed throughout macroscopic postpeak deformation, highlighting the spatial nonuniformity of shear band kinematics. Local volumetric strains are integrated and averaged over the shear band region to enable comparison with global behavior. Finally, the periodicity of observed kinematic fluctuations at the softening-critical state transition is analyzed to provide preliminary insight toward an internal material length scale.

2. EXPERIMENTAL METHODS

Prismatic-shaped (14 by 4 by 8 cm) sand specimens are subjected to plane strain compression (Figure 1). Glass-lined acrylic plates enforce the zero-strain conditions and allow imaging of in-plane deformations. The glass wall-sand membrane interface is lubricated with translucent silicon oil to minimize frictional loss. The specimen base rests on a low-friction linear bearing "sled," which provides the kinematic freedom for translation and offset required for unconstrained formation of a single persistent shear band. Specimens are sealed within a translucent latex membrane. The configuration shown in Figure 1 is mounted within a 41-cm diameter, 3.175-cm-thick acrylic confining cell that is filled with 10 cSt. pure silicon fluid to provide the medium for confining pressure (in plane horizontal stress) application. This apparatus also has been described in previous works, where the reader is referred for more information (e.g. [2,13,21]).

Two different subrounded to subangular sands are represented in the results presented here. The first, called "Masonry-Coarse" (MC) sand, is a sieved uniform mixture of masonry and construction sands: D_{50}=0.84 mm, C_u=1.2, and C_c=1.1. Results are also presented for uniform sieved Delaware Beach (DB) sand: D_{50}=0.40 mm, C_u=1.3, and C_c=1.1. These sands were mixed and/or chosen to create a varied grain coloring to reflect gray-level variation in the digital images, which is a requirement for use of the DIC technique as described below. Specimens were prepared by allowing

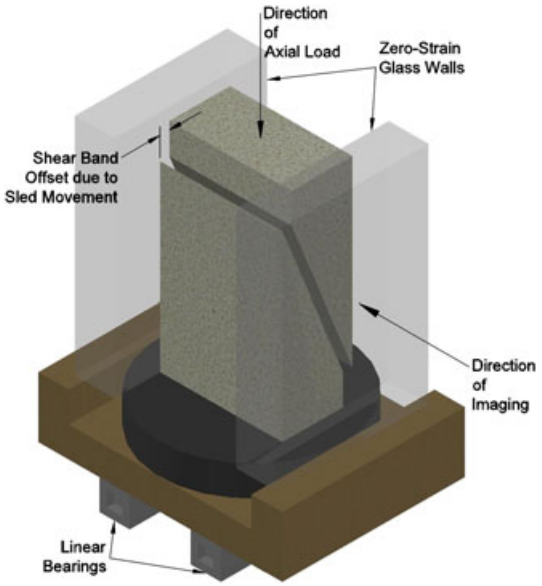

Figure 1. Concept drawing depicting key features of the plane strain testing apparatus.

dry sand to free-fall through a rainer of a slightly smaller footprint as the specimen. Multiple openings in the rainer, followed by a coarse mesh, helped distribute the sand uniformly across the specimen cross section. Specimen relative densities typically ranged between approximately 75 and 100%, and consolidated mean normal effective stresses were kept correspondingly low, 110 to 200 kPa, to promote dilative response and shear band formation. Specimens were saturated and sheared under drained strain-controlled compression.

Throughout shearing, digital images were collected at regular intervals, typically every 0.10 to 0.2% global axial strain. Note that the radius of curvature of the acrylic confining cell is locally relatively large, so image distortion across the 4-cm specimen width has been found to be negligible [27].

3. DIGITAL IMAGE CORRELATION

The DIC method derives displacements by mapping subsets of pixels at many points across the specimen surface (e.g. [28,29]). The result is a very fine and nearly temporally continuous (based on rate of image capture) representation of grain-scale surface motion. Here, we offer only a brief overview of the DIC method, so the reader is referred to the above references for more in-depth coverage of the topic. The software VIC-2D, by Correlated Solutions, Inc., was used to execute the DIC measurements.

A typical 8-bit digital image represents a two-dimensional array of gray-level values, which are integers ranging from 0 (pure black) to 255 (pure white). For an object whose surface is varied in terms of coloring, pixel gray-level values will vary spatially. Between consecutive images depicting a deformation process, local displacement are obtained by mathematically mapping gray-level patterns within small subsets of pixels. Here, the Normalized Sum Square Difference (NSSD) coefficient is utilized as the minimization measure in the subset mapping process. The output of DIC are the displacements of the subset centers, and by overlapping subsets, an intense spatial array of local displacement data is obtained.

Two different experimental grade digital cameras were used to collect the images: a 4-Megapixel Q-Imaging PMI 4201 camera and a 5-Megapixel Point Grey Grasshopper camera. Note that camera sensors must be of "experimental grade" (zero or very low defect), as a given feature, or "speckle," as it translates from pixel to pixel, which must yield a consistent gray-level for accurate DIC-based mapping. Typically, image scales were around 17 pixels/mm (or 0.06 mm/pixels), such that a 0.4-mm-diameter sand grain occupies about 7 pixels across. Having an image feature, here, a sand grain occupies multiple pixels is known as "oversampling" and is needed for subpixel displacement measurement accuracy (e.g. [30]). Subpixel displacement measurement is further enabled by interpolating pixel gray-level values between pixels to create a smooth representation of gray-level variation. Cubic b-spline interpolations were used here.

The accommodation of surface straining is essential for accurate DIC mapping. In the case of sands, slight relative movement among the sand grains (over small deformation increments) manifests such straining. Subset straining typically is accommodated in DIC by including an assumed form of subset deformation shape functions in the mapping minimization measure. For example, if $\boldsymbol{x}$ represents the initial position of some point within a subset, and $\boldsymbol{x}'$ represents the corresponding deformed position of the same point, then for first-order subset straining [31], we have

$$\left(x^{'}\right)_i = (x)_i + (u)_i + \frac{\partial\{u_i(\mathrm{x})\}}{\partial x_j} dx_j, \tag{1}$$

where $\boldsymbol{u}$ is the vector displacement field, $i, j=1, 2$ (for 2D), and $\partial u_i/\partial x_j$ are the displacement gradients of the subset. Thus, minimization of the NSSD coefficient, and thus accurate displacement measurement, depends not only on displacement, $\boldsymbol{u}$, but also on the strain the subset is assumed to undergo. Herein, image increments of 0.1 to 0.2% axial strain, which represent about 2 to 4% gross shear strain across a shear band, proved adequate to accurately accommodate the assumption of first-order subset deformation. While the subset shape functions can provide a measure of local straining, it is more accurate to calculate local strains directly from the displacement field (e.g. [32,33]). We note that other recent implementations of DIC for granular material analysis [24,34] seem to not have explicitly accommodated the possibility of subset deformation in the DIC matching algorithms. Not accommodating

subset straining is a potentially significant omission: if the material is undergoing strain, undermatched subset shape functions can lead to systematic errors [35].

Subset sizes should be large enough to reflect a unique gray-level variation but small enough to allow capturing of strain nonuniformity within the material. The latter was the overriding consideration here. A systematic trial was performed, and for subset sizes smaller than about 10 times the median grain diameter, D_{50} (or, about the thickness of the shear band), spatial variations in displacement and strain along the shear band were consistently detected, independent of subset size. Subsets that were larger than about 10 times D_{50}, on the other hand, tended to average out kinematical behavioral fluctuations, giving the impression of more uniform deformation. Thus, to ensure precise detection and characterization of shear band spatial behavioral nonuniformities, subset sizes were routinely kept smaller than 10 times D_{50}. Subset center-to-center spacing was scaled to achieve displacement data point spacing on the order of median grain diameter. DIC measurement accuracy has been found to be about +/− 0.009 mm.

Figure 2 shows contours of displacement norm obtained from a typical DIC analysis conducted between two images representing a 0.6% axial strain increment after a shear band had fully formed (note that while such relatively large strain increment leads to displacement measurement inaccuracies amidst the assumption of first-order subset deformation, it is used here to qualitatively illustrate the nature of the macroscopic deformation field). The material above the shear band is seen to be translating vertically downward with the applied axial load, the material below the shear band translates laterally with the base "sled," and nonzero displacement gradients are seen only within the shear band. The DIC analysis reflected in Figure 2 comprised about 10,000 displacement data points over the entire analysis area and about 600 data points within the shear band.

4. DISPLACEMENTS AND KINEMATICS IN A LAGRANGIAN FRAME

As described above, the DIC method enables very accurate computation of local *incremental* displacements across an object's surface between digital images taken at two different instances in time during a deformation process. Previous research [13] has indicated that force chains collapse over

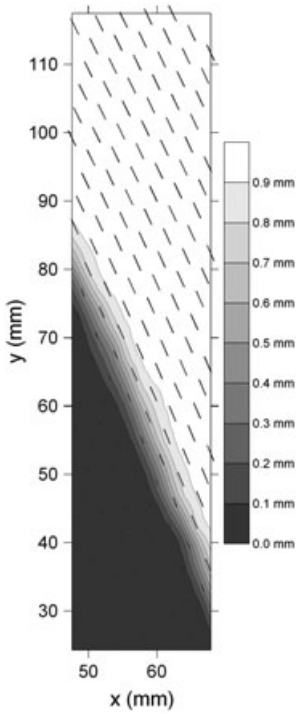

Figure 2. Typical DIC-measured displacement field (referenced to base sled) after full shear band formation. Scaled displacement vectors are shown at selected locations indicating the general direction of motion.

larger strain increments that are afforded by our DIC analyses increments here. The task then is to devise a means to accurately accumulate successive DIC results to enable characterization of large-deformation, local shear band displacements, and ensuing strain and kinematic behaviors that serve as signatures of force chain collapse. Because several commercial DIC codes have now incorporated accumulation methodologies, descriptions of procedures underlying such methodologies are of interest. Here, we first describe the approach developed to accumulate successive DIC results. We then describe the strain and kinematic measures that will be used to characterize behavior over finite deformation increments.

Figure 3 conceptually depicts the accumulation process for two consecutive deformation increments. Figure 3a shows image i of an arbitrary object (here represented with a checkerboard pattern for ease in visualization) at some initial deformation state. The black dots represent locations of subset centers, $\mathbf{x}_i^{sp}$, spaced on a regular grid. Here, the superscript "sp" emphasizes a spatial (Eulerian) reference frame. Note that the sizes of the subsets (not shown) are typically much larger than the grid-point spacing. The "triangles" in Figure 3a represent the deformed positions, $\mathbf{x}_{i+1}$, of the subset centers obtained from a DIC analysis of images i to $i+1$ (only upper-left four data points are shown for clarity):

$$x_{i+1} = x_i^{sp} + \Delta u_{i\rightarrow i+1}^{sp}, \tag{2}$$

where $\Delta u_{i\rightarrow i+1}^{sp}$ represents the DIC-measured displacements of $\mathbf{x}_i^{sp}$ between images i to $i+1$.

Figure 3b shows the deformed state of the same object in Figure 3a as captured by image $i+1$. Note that the deformations are intentionally shown to be large for visualization purposes only. Our goal here is to track the positions of the "triangles," $\mathbf{x}_{i+1}$, as they move in the subsequent deformation increment, from image $i+1$ to $i+2$. We first use DIC to measure incremental displacements, $\Delta u_{i+1\rightarrow i+2}^{sp}$, of spatial grid points, $\mathbf{x}_{i+1}^{sp}$, the positions of which may or may not be the same as in previous DIC increments (for demonstration purposes, the grid of subset centers in Figure 3b is shifted slightly, in image coordinate space, from that in Figure 3a). Then, to track the fate of the triangles, we must interpolate the DIC result, $\Delta u_{i+1\rightarrow i+2}^{sp}$, at the correct locations, points $\boldsymbol{x}_{i+1}$. We employ the cubic spline interpolation method here. While the nature of the displacement field between subset centers is not known a priori, we suspect it is likely nonlinear within a shear band, even for small strain increments. Note that the accumulation approach used by Gonzales and Knauss [36] for application to a bonded continuous solid utilized a linear interpolation.

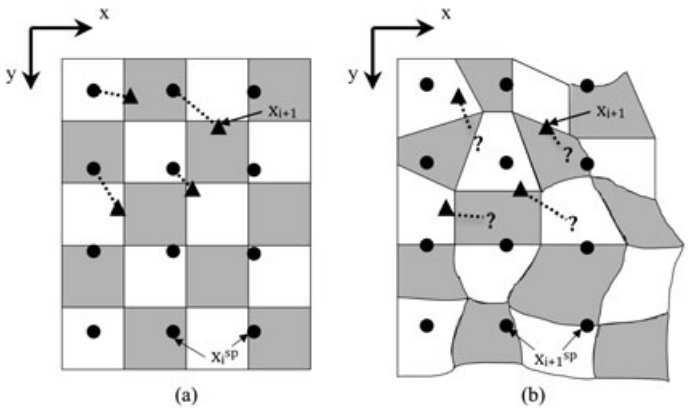

Figure 3. Process of accumulating successive DIC results: a) image i, representing an arbitrary initial state of a checkerboard-colored object; and b) image i+1, representing a subsequent deformation state. The origin of the "global" or image coordinate system, anchored to the fixed camera, is indicated at the upper left of each image. Solid dots represent the regular grid of subset centers (the subsets themselves are not shown). Triangles in (a) represent deformed positions, x, of subsets centers for the deformation increment i to i+1. The same triangles are shown in (b); we wish to track their displacement for the increment i+1 to i+2, based on DIC-measured displacements of the subset grids, x_{i+1}^{sp}.

In general, if the grid points in Figure 3a represent material points, $\mathbf{X}$, whose displacements we wish to track through n DIC increments, then the accumulated Lagrangian displacement field, $\mathbf{u}_n$, is given as

$$\mathbf{u}_n = \mathbf{u}_1 + \sum_{k=2}^{n} \Delta\mathbf{u}_k, \tag{3}$$

where $\Delta\mathbf{u}_k$ represent the interpolated incremental displacements of the material coordinates during the kth DIC analysis increment. Note that no interpolation is required for $\mathbf{u}_1$ because the displacements of $\mathbf{X}$ are analyzed directly.

The deformation gradient over the accumulated n increments can be determined directly by

$$\mathrm{F}_n = \mathrm{I} + \frac{\partial \mathrm{u}_n}{\partial \mathrm{X}}, \tag{4}$$

where the accumulated displacement $\mathbf{u}_\mathrm{n}$ is differentiated with respect to the Lagrangian grid, $\mathbf{X}$. The deformation gradient could also be determined from the deformation gradient increments, as in Gonzales and Knauss [35]. Consider two DIC analyses performed on two consecutive sets of images, (I_0, I_1) and (I_1, I_2). The accumulated displacement over the two increments, $\mathbf{u}_2$, is a function of $\Delta u_{0\to1}$ and $\Delta u_{1\to2}$, which respectively depend on x_0, the initial material coordinates, and x_1, the material coordinates after $\Delta u_{0\to1}$. Then, the deformation gradient after these n=2 increments is

$$\mathrm{F}_2 = \mathrm{I} + \frac{\partial \mathrm{u}_2}{\partial \mathrm{x}_0} = \mathrm{I} + \frac{\partial(\Delta \mathrm{u}_{1\to2} + \Delta \mathrm{u}_{0\to1})}{\partial \mathrm{x}_0}. \tag{5}$$

Taking into account the chain rule in the calculation of $\partial \Delta u_{1\to2}/\partial \mathrm{x}_0$,

$$\frac{\partial \Delta \mathbf{u}_{1\to2}}{\partial \mathbf{x}_0} = \frac{\partial \Delta \mathbf{u}_{1\to2}}{\partial \mathbf{x}_1} \cdot \frac{\partial \mathbf{x}_1}{\partial \mathbf{x}_0}, \tag{6}$$

Equation 5 becomes

$$\mathrm{F}_2 = \mathrm{I} + \frac{\partial \Delta \mathrm{u}_{1\to2}}{\partial \mathrm{x}_1} \cdot \left(\mathrm{I} + \frac{\partial \Delta \mathrm{u}_{0\to1}}{\partial \mathrm{x}_0}\right) + \frac{\partial \Delta \mathrm{u}_{0\to1}}{\partial \mathrm{x}_0} = \left(\mathrm{I} + \frac{\partial \Delta \mathrm{u}_{1\to2}}{\partial \mathrm{x}_1}\right) \cdot \left(\mathrm{I} + \frac{\partial \Delta \mathrm{u}_{0\to1}}{\partial \mathrm{x}_0}\right), \tag{7}$$

which is reduced to

$$\mathrm{F}_2 = \Delta\mathrm{F}_{1\to2} \cdot \Delta\mathrm{F}_{0\to1}, \tag{8}$$

where $\Delta\mathrm{F}_{i\to i+1}$is the incremental deformation gradient from image i to $i+1$:

$$\Delta\mathrm{F}_{i\to i+1} = \mathrm{I} + \frac{\partial \mathrm{u}_{i\to i+1}}{\partial \mathrm{x}_i}. \tag{9}$$

The generalization of Eqn 8 for n image increments is

$$\mathrm{F}_n = \prod_{k=1}^{n} \Delta\mathrm{F}_k. \tag{10}$$

Note, however, that the incremental deformation gradients, $\Delta\mathrm{F}_k$, must be computed with respect to the current material coordinates, $\mathbf{x}$, which are not on a regular grid. Alternatively, $\Delta\mathrm{F}_k$ can be computed with respect to $\mathbf{x}^{\mathrm{sp}}$, but then, it must be interpolated properly at $\mathbf{x}$ before running the product

in Eqn 10. For convenience, Eqn 4 was used here, as no additional interpolation is required. Derivatives in the present paper are obtained by central differences, which are second-order accurate in space.

We utilize several kinematic quantities, derived from the deformation gradient to characterize mesoscale activity within shear bands. Macrorotations that correspond to rigid body rotations can be obtained from the polar decomposition of **F** (here, we refer to the accumulated **F**, but the subscript is dropped for convenience). **F** is decomposed in terms of an orthogonal rotation tensor **R** and a symmetric stretch tensor, **U**, in the material configuration:

$$\mathrm{U} = \sum_{\alpha=1}^{3} \lambda_\alpha \mathrm{N}_\alpha \otimes \mathrm{N}_\alpha, \tag{11}$$

in which $\mathbf{N}_1$, $\mathbf{N}_2$, and $\mathbf{N}_3$ are the eigenvectors of the right Cauchy-Green tensor, $\mathrm{C}=\mathrm{F}^T\cdot\mathrm{F}$, and ${\lambda_1}^2$, ${\lambda_2}^2$, and ${\lambda_3}^2$ are the corresponding eigenvalues (e.g. [37]). Note that, for plane strain, $\lambda_3=0$. Then, $\mathrm{R}=\mathrm{F}\cdot\mathrm{U}^{-1}$, and the subsequent rotation Ω is calculated from

$$\mathbf{R} = \begin{bmatrix} \cos\Omega & \sin\Omega & 0 \\ -\sin\Omega & \cos\Omega & 0 \\ 0 & 0 & 1 \end{bmatrix}. \tag{12}$$

Area changes at the surface of the specimen are also computed. Because out-of-plane translation of sand grains from the imaging surface is only occasionally observed, we assume that the area changes on the surface are reflective of volume change. Thus, local volume change is characterized from

$$dV_n = J_n dV_o, \tag{13}$$

where dV_o represents the infinitesimal material volume at the beginning of the accumulated increment, dV_n the volume after the accumulation of n DIC increments, and $J_n=\det(\mathbf{F}_\mathrm{n})$.

The scalar quantities Ω and J, derived from finite strain accumulations, will be used below to characterize kinematic activity within shear bands. For convenience, we will translate our data interpretation to the shear band basis, with axes x^* and y^* running parallel and perpendicular to the shear band, respectively. To obtain the inclination of the shear band, we utilize the velocity gradient, $\mathbf{L} = \partial\mathbf{v}(\mathbf{x},t)/\partial\mathbf{x}$. Assuming that only points within the shear band are subject to significant nonzero velocity gradient (see Figure 2), we apply a small threshold on $|\mathbf{L}|$ to isolate points considered to be part of the shear band, and then, shear band inclination is obtained by a least squares linear fit to those points. We emphasize that the kinematic quantities reported here are derived from the calculation of the relative movements between adjacent subset centers (spaced on the order of a sand grain) and are not reflective of the kinematic behavior of the DIC subsets or individual sand grains.

5. ACCURACY OF ACCUMULATED DEFORMATIONS

To assess the accuracy of our accumulation approach, we accumulate displacements in the uniformly translating regions above and below the shear band (Figure 2) and compare with corresponding displacements measured from linear variable differential transformer (LVDT) transducers located inside the confining cell. First, vertical translation of the top platen is compared with vertical displacements of the top row data of the DIC analysis data, adjacent to the top platen; second, horizontal movements of the linear bearing "sled" are compared with the bottom row of DIC data, just above the sled. As subset straining is zero in these regions, DIC analyses can also be performed quite accurately over large deformation increments. Thus, "direct" DIC measurements were used as an additional check against the accumulated results.

A test on dense Delaware Beach (DB) sand was used for comparison. Global response data for this test are shown in Figure 4. The data points on the shear stress, q, versus axial strain curve indicate locations where relevant images were collected. Corresponding image numbers are noted next to a few

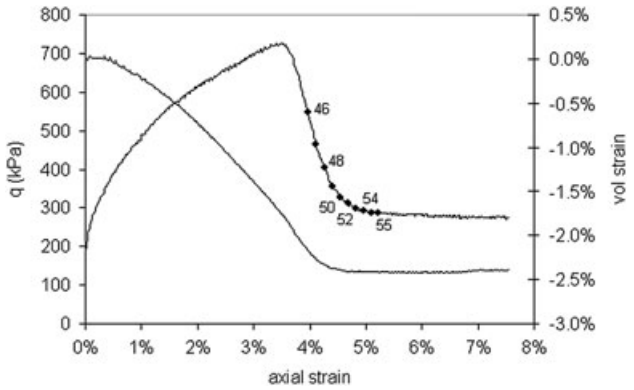

Figure 4. Global shear stress and volumetric strain response of a dense DB sand during a drained plane strain compression test.

of the points for reference. The axial strain increment, $\Delta\varepsilon_a$, between each consecutive image was around 0.14 to 0.15%. We start with deformation analyses between images 46–47 and successively consider larger and larger strain increments, e.g. 46–48, 46–49, etc., up to 46–52, which represents a maximum axial strain increment of 0.87% (larger strain increments are not of interest, as will be discussed below). Figure 5 shows the corresponding displacement measurements as a function of axial strain increment. For both the horizontal (Figure 5a) and vertical (Figure 5b) displacements, the accumulated deformations are determined in accordance with the other measurement sources with nearly negligible difference for increments at least up to $\Delta\varepsilon_a \approx 0.75\%$. At $\Delta\varepsilon_a=0.87\%$, and the accumulated results begin to differ, albeit only slightly, while it is not shown here that increments up to $\Delta\varepsilon_a=1.14\%$ were analyzed with little additional error. Herein, accumulated increments were typically around 0.6% axial strain.

6. VALIDATION OF LARGE STRAIN MEASURES

To gage the nature of straining within shear bands and to emphasize the need for a large strain formulation, we compare the rigid rotation, Ω, computed from the rotation tensor $\mathbf{R}$ (Eqn. 12) to its infinitesimal equivalent, ω, for a variety of accumulated strain increments. The same DB sand test as above is again used for this comparison (Figure 4). The comparison between Ω and ω is conducted for three different axial strain increments, 0.15%, 0.59%, and 1.27%, represented respectively by the

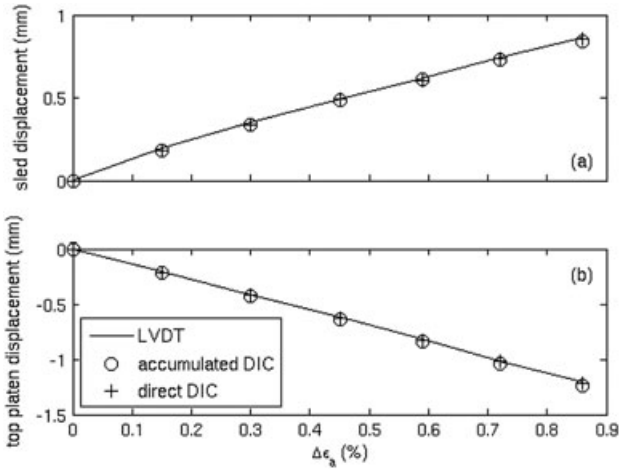

Figure 5. Comparison among accumulated DIC, direct DIC, and LVDT-measured displacements for (a) horizontal translations adjacent to the bottom "sled," (b) vertical translations adjacent to the top platen.

image increments 46–47, 46–50 and 46–55 (note that force chains are in the process of buckling through the course of softening and the softening-critical state transition [13]; thus, significant nonzero rotation should be present in each of these increments). Incremental DIC analyses are conducted between each consecutive image pair, e.g. 46–47, 47–48, etc., and then, corresponding accumulations were performed. The deformation gradient, $\mathbf{F}$, and, then, Ω and ω each were computed over the corresponding accumulated increments.

We define the relative difference between finite and infinitesimal rotations as:

$$\Delta\Omega_{\text{inf}} = \frac{\Omega - \omega}{\Omega}. \tag{14}$$

A fixed number of displacement data points (582) inside the shear band were used for each calculation. Figures 6a through 6c shows the frequency distributions of $\Delta\Omega_{\text{inf}}$, expressed as percentages, for the three respective strain increments. For $\Delta\varepsilon_a$=0.15% (Figure 6a), the relative difference between finite and infinitesimal rotations is less than 1% for approximately 80% of the 582 data points, and the maximum difference is less than 2%. However, as axial strain increment increases, not only does the mean relative difference increase, but the spread in relative difference also increases. For $\Delta\varepsilon_a$=1.27% (Figure 6c), the average $\Delta\Omega_{\text{inf}}$ is 4.5%; and, for more than 40% of the data points, the calculated differences are between 5 and 12% (Figure 6d). Note that part of the increased spread in relative difference in Figures 6a to 6c is because of the significant spatial variation in kinematic activity along the shear band that arises in the latter parts of softening [13].

The results in Figure 6 clearly justify the use of finite strain measures for representing shear band kinematics, in particular for deformation increments greater than 0.15% global axial strain ($\approx$2 to 4% gross shear strain). Because the spatial regions where rotational magnitudes are highest likely signify force chain buckling, an accurate characterization of the spatial variation in kinematic activity, and consequently force chain spacing, is crucial for proper behavioral characterization and potential length scale assessment associated with granular material deformation.

Further glimpse on the nature of straining within a shear band, and the limitations of the DIC technique when used over large strain increments, we compare finite strain rotation, Ω, calculated from accumulated DIC measurements to rotation calculated from a single direct DIC analysis performed directly over the same strain increment, Ω_{direct}. For the former, we use the accumulated data for the strain increment $\Delta\varepsilon_a$=0.59% described above. For the latter, we perform a DIC analysis directly from images 46–50 and calculate Ω_{direct} for the same 582 points within the shear band as in the accumulated results. We define the relative difference between the two methods, $\Delta\Omega_{\text{dir}}$, in a similar fashion as

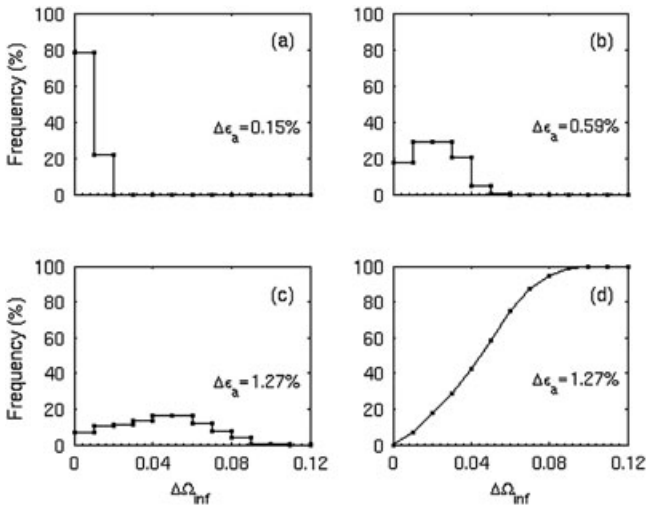

Figure 6. Frequency distributions ((a) through (c)) and cumulative distribution function (d) of the relative difference between finite and infinitesimal rotations within the shear band as a function of strain increment.

Eqn 14 but with ω replaced by Ω_{direct}. Figure 7 presents the frequency and cumulative (inset) distribution functions for $\Delta\Omega_{dir}$. The results show significant spread in $\Delta\Omega_{dir}$, which locally can be as high as 60%. For about 30% of the data points, the difference exceeds 5%. The results in Figure 7 emphasize the necessity of accumulating incremental DIC results for precise shear-band behavioral characterization over large strains.

7. VOLUMETRIC STRAIN NONUNIFORMITY IN SHEAR BANDS

We utilize the accumulation procedure described above to examine the nature and evolution of kinematic volumetric activity within a persistent shear band, with a particular focus on spatial nonuniformity and patterning. Our analyses were foremost targeted with the aim of most distinctly capturing the kinematic pattern seen at the softening-critical-state transition by Rechenmacher *et al.* [13], which, again, is indicative of a coordinated force chain buckling event. Based on trial and error, we have found that gross shear band shear strain increments of roughly 10 to 15% most optimally capture the kinematic fluctuations associated with this force chain collapse event (see [13]). These increments formed the starting point for the analyses shown here.

Figure 8 shows spatial variations in the Jacobian, J (Eqn. 13), along and surrounding a persistent shear band, and their evolutions through macroscopic postpeak deformation during a plane strain compression test on a dense MC sand specimen (Figure 9). Figures 8a through d each represent behavior over an axial strain increment of approximately 0.6% (≈14% gross shear strain across band) derived from an accumulation of DIC results over three consecutive 0.2% axial strain DIC increments. The data points in Figure 9 demarcate the position with respect to macroscopic behavior of the first and last images in each 0.6%-accumulated increment (image numbers are labeled only in Figure 9a for clarity). The first accumulated strain increment (Figure 8a), between images 64–70, represents the initial stages of softening, just after full shear band formation. The specimen globally is dilating (Figure 9). Similar behavior is reflected locally in the Jacobian data in Figure 8a, and dilation magnitude is largely uniform along the length of the shear band. In the next strain increment, represented between images 70–76, the sand is still undergoing macroscopic softening. Both global and local dilation have lessened in magnitude, as compared to the previous increment. Locally, few zones along the shear band began to exhibit contraction (Figure 8b). The third increment, reflected between images 76–82, is at the softening-critical-state transition. Global volume change is nearly zero, and yet, Figure 8c indicates that significant nonzero volumetric activity is occurring locally within the shear band: contractive and dilative behavior alternate in nearly periodic fashion spatially along the length of the shear band. Such behavior is a direct manifestation of the coordinated

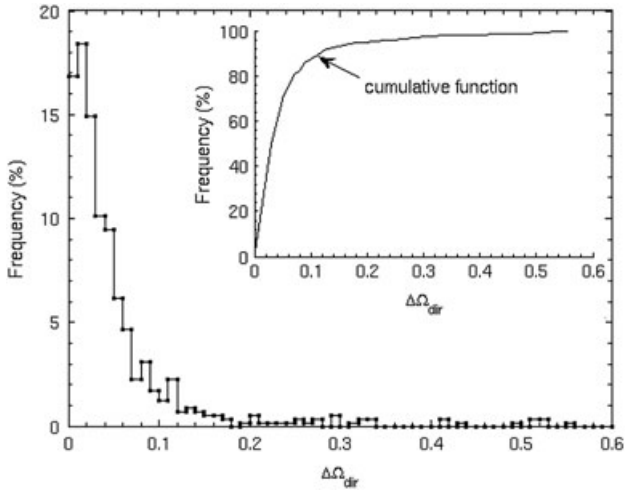

Figure 7. Frequency and cumulative (inset) distributions for differences between finite-strain rotations calculated from accumulated versus direct DIC analyses over 0.59% axial strain increment.

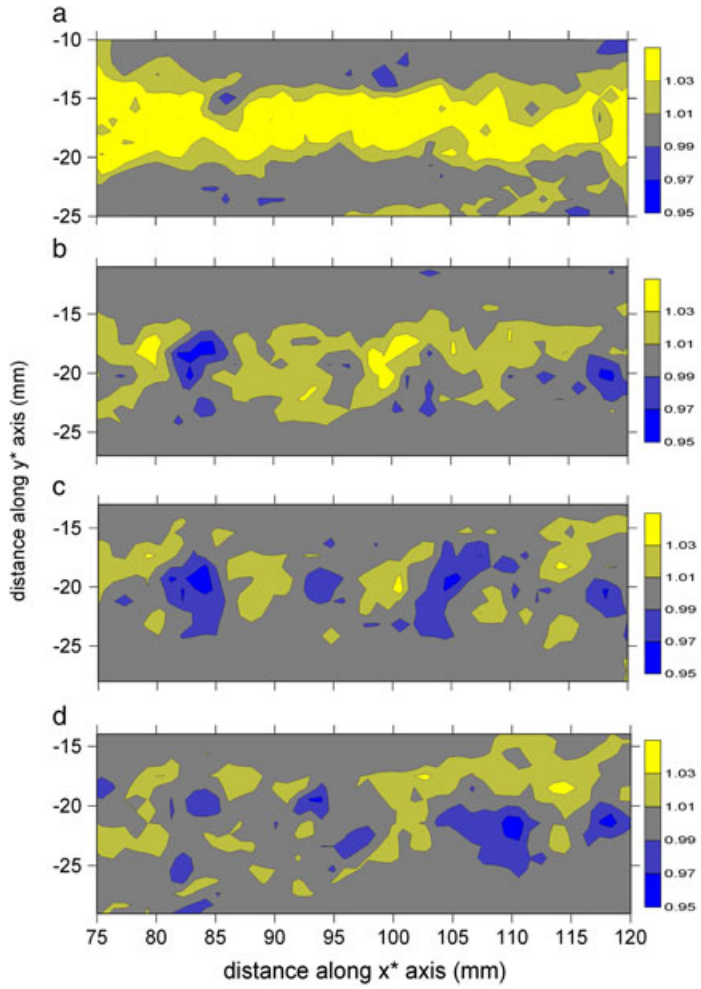

Figure 8. Local shear band volumetric strains for a dense MC sand specimen calculated from accumulations over the following axial strain increments: (a) 6.3 to 7.0%, (b) 7.0–7.6, (c) 7.6–8.3, (d) 8.3–8.9 (see Figure 9). Light colors (yellow online) represent dilation ($J>1$) and dark colors (blue online) represent contraction ($J<1$).

multiforce chain buckling identified by Rechenmacher *et al*. [13]. We emphasize again that the strain increment of analysis represented in Figure 8c was not stumbled upon randomly: it was settled on after many extensive trials of different windows, and thus we feel it fairly accurately represents the typical duration of this force chain buckling event. The final increment, between images 82–88, is entirely within the critical state: shear stress is approximately constant and global volumetric strain is approximately zero (note that the minor global volumetric contraction near the end of the test was performed because of a small leak that formed in the specimen drainage line). Nevertheless, local volumetric contraction and dilation (Figure 8d) are still occurring along the shear band, though in a less patterned fashion as the previous increment. Note that through all increments, local volume change outside of the shear band is practically zero.

Because global volumetric strain is nearly zero for the strain increments reflected in Figures 8c and d, the expansion and contraction observed along the shear bands should balance each other. As an additional means to validate the nature of our DIC-derived accumulated volumetric behavior, we integrate and average the calculated local J values across the shear band and compare it to the global volumetric strain measured for the same analysis increments. The boundaries of the shear band are approximated by way of the displacement gradient: regions of nonzero displacement gradient (above a small threshold) are considered to be inside the shear band. The volumetric strain, ε_{vol}, then is calculated from $\varepsilon_{vol}=1-J$. Table I compares the integrated local and global volumetric strains for each

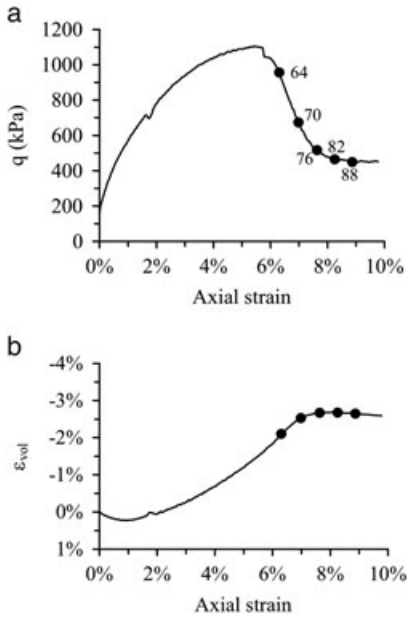

Figure 9. Global shear stress (top) and volumetric strain (bottom) versus global axial strain during a plane strain compression test on dense MC sand. Data points indicate the first and last image numbers corresponding to the accumulated increments in Figure 8. Image locations/numbers in (b) are same as in (a). The "bumps" in the curves at approximately 2.0 and 5.5% axial strain were because of an errant fluctuation in sensor readings. The slight volumetric compression during critical state was because of a very small leak in the specimen drainage line.

analysis increment. During softening (image increments 64–70 and 70–76), volumetric strain within the shear band is significantly higher than it was captured globally. Mooney *et al*. [8] and Finno and Rechenmacher [2] similarly saw differences between local and global dilative volumetric strain magnitudes within shear bands. Nearer to and during the critical state (image increments 76–82 and 82–88), both global and local measurements reflect minimal volume change. Note that the values of local ε_{vol} reported in Table I depend on the threshold used to assess the shear band limits; however, this dependency is on the order of (10^{-2}) % of volumetric strain. Further, while the critical state local (integrated) volumetric strain magnitudes of −0.06 and −0.11% may seem significant as compared to global magnitudes recorded during softening, they represent less than 3% of the *integrated* volumetric strain (−3.53%) that occurred during softening. From this standpoint, the shear band can be considered to be deforming at constant volume. This general agreement between the integrated local and global volumetric strains serves to further validate the precision of our accumulation approach. Moreover, the results in Figures 8 and 9 and Table I quantitatively confirm that a global critical state of continual shearing at constant volume had been achieved in the shear band only in an average sense: locally, the shear band material is undergoing significant nonzero volumetric strain. This observation suggests that the traditional definition of "critical state" does not accurately describe true material behavior, at least during the initial stages of critical state that were analyzed here.

Table I. Postpeak incremental global and local (accumulated shear band only) volumetric strains during a plane strain test on dense MC sand (Figure 9).

Image increment	Axial strain increment (%)	Global volumetric strain (%)	Integrated local volumetric strain (%)
64–70	6.3–7.0	−0.44	−3.53
70–76	7.0–7.6	−0.14	−0.66
76–82	7.6–8.3	0.00	−0.06
82–88	8.3–8.9	+0.03	−0.11

The need for accumulating incremental DIC results was clearly justified in Sections 5 and 6. However, to directly assess the effect of large-strain DIC analysis (i.e. without accumulation) on computed volumetric behavior, we performed a DIC analysis directly from images 76 to 82 and compared the computed Jacobian, J, with the accumulated result shown in Figure 8c. Both analyses produced a very similar pattern of J variation along the shear band. However, consistently, the DIC-direct analyses overpredicted J magnitudes, translating to local over-predictions in volumetric strain, which in some cases is as high as 50%. Similar comparisons of our tests yielded similar results. These observations further emphasize the need for accumulation approaches for accurate assessment of mesoscale granular material response using DIC methods.

At the softening-critical-state transition, Rechenmacher *et al*. [13] found a pattern of Jacobian variation similar to that in Figure 8c, which, again, has been shown to represent the kinematic manifestation of a coordinated multiforce chain collapse event. The seemingly periodic variation in the pattern, seen here as well as in [13] and [25], is striking. The spacing between successive peaks in Figure 8c was contrasted with pattern spacing observed in the works cited above, each representing behavior for different sands [38]. Preliminarily, it seems that pattern spacing increases with median grain size; however, the increase is not linear, which is not surprising, given the subtle differences among the sands: the sand tested here was subrounded, the sand in [13] was more subangular, and the data by Rechenmacher [25] was derived from more well-graded sand (C_u=3.8). Thus, other factors besides median grain size are likely at play, and the precise nature of any such correlation will require more data. Regardless, that kinematic spacing and grain size do correlate emphasizes the nonrandom nature of the observed kinematic patterns. Given the important implications for finding an underlying physically based internal length scale governing granular material deformation, these findings merit additional research, and the techniques described here will serve an important role in this effort.

8. CONCLUSIONS

The experimental method of DIC has been employed to quantify local displacements, for grain scale resolution, within shear bands in sands undergoing plane strain compression. A methodology has been presented to accumulate incremental DIC analysis results to afford displacement measurements over large strain increments. Comparison of the accumulated deformations in uniformly translating zones with external deformation measures have been used to validate the accuracy of the proposed accumulation method. Comparison between kinematic rotations derived from large strain and infinitesimal approximations legitimize the choice of large strain measures used herein and additionally highlight the nature of the significant straining that occurs locally within shear bands.

The accumulation methodology was used to track the spatial variation of volumetric strain within a shear band throughout the postpeak regime. Volumetric strain was seen to evolve from fully dilative to spatially varying dilation and contraction. Integration of the volumetric strain variations across the shear band within deformation increments during the global critical state confirms the material volumetric strain is indeed zero during the critical state. These results further legitimize the DIC-based accumulation approach offered here for local strain characterization in sands. The local volumetric fluctuations seen during the global critical state suggest that the traditional definition of critical state is not sufficient to describe local material behavior.

At the softening-critical-state transition, previous research has revealed a clear pattern of nearly periodic spatial variation of various kinematic quantities. The volumetric strain fluctuations presented here exhibit similar spatial variation. Comparison of the spatial periodicity found among several tests suggests that the spatial patterning depends at least in part on grain size and that this spacing may reflect an internal length scale that merits further consideration, for which the techniques described here will play an important role.

ACKNOWLEDGEMENTS

The authors would sincerely like to thank the National Science Foundation (grant CMMI-0748284) and the University of Southern California for their financial support of this research.

REFERENCES

1. Finno RJ, Harris WW, Mooney MA, Viggiani G. Shear Bands in Plane Strain Compression of Loose Sand. *Geotechnique* 1997; **47**(1):149–165.
2. Rechenmacher AL, Finno RJ. Digital image correlation to evaluate shear banding in dilative sands. *Geotechnical Testing Journal* 2004; **27**(1):13–22.
3. Bardet JP, Proubet J. A numerical investigation of the structure of persistent shear bands in granular media. *Geotechnique* 1991; **41**(4):599–613.
4. Tejchman J, Bauer E. Numerical simulation of shear band formation with a polar hypoplastic constitutive model. *Computers and Geotechnics* 1996; **19**(3):221–44.
5. Iwashita K, Oda M. Micro-deformation mechanisms of shear banding process based on modified distinct element method. *Powder Technology* 2000; **109**(1–3):192–205.
6. Thornton, Zhang L. A numerical examination of shear banding and simple shear non-coaxial flow rules. *Philsophical Magazine* 2006; **86**(20–21):3425–3452.
7. Desrues J, Chambon R, Mokni M, Mazerolle F. Void Ratio Evolution Inside Shear Bands in Triaxial Sand Specimens Studied by Computed Tomography. *Geotechnique* 1996; **46**(3):529–546.
8. Mooney MA, Finno RJ, Viggiani G. A Unique Critical State for a Sand? *Journal of Geotechnical and Geoenvironmental Engineering* 1998; **124**(11):1100–1108.
9. Finno RJ, Rechenmacher AL. Effects of consolidation history on critical state of sand. *Journal of Geotechnical and Geoenvironmental Engineering* 2003; **129**(4):350–360.
10. Evans TM, Frost JD. Multiscale investigation of shear bands in sand: Physical and numerical experiments. *International Journal for Numerical and Analytical Methods in Geomechanics* 2010; DOI: 10.1002/nag.877.
11. Oda M, Kazama H. Microstructure of shear bands and its relation to the mechanisms of dilatancy and failure of dense granular soils. *Geotechnique* 1998; **48**(4):465–481.
12. Utter B, Behringer RP. Experimental measures of affine and nonaffine deformation in granular shear. *Physical Review Letters* 2008; **100**(20), 208302-1-4.
13. Rechenmacher A, Abedi S, Chupin O. Evolution of Force Chains in Shear Bands in Sand. *Geotechnique* 2010; **60**(5):343–351.
14. Oda M, Iwashita K. Study on couple stress and shear band development in granular media based on numerical simulation analysis. *International Journal of Engineering Science* 2000; **38**(15):1713–1740.
15. Arslan H, Sture S. Evaluation of a physical length scale for granular materials. *Computational Materials Science* 2008; **42**(3):525–530.
16. Tordesillas A, Muthuswamy M, Walsh SDC. Mesoscale Measures of Nonaffine Deformation in Dense Granular Assemblies. *Journal of Engineering Mechanics* 2008; **134**(12):1095–1113.
17. Tordesillas A, Muthuswamy M. On the modeling of confined buckling of force chains. *Journal of the Mechanics and Physics of Solids* 2009; **57**(4):706–727.
18. Alonso-Marroquin F, Vardoulakis I, Herrmann HJ, Weatherley D, Mora P. Effect of rolling on dissipation in fault gouges. *Physical Review E* 2006; **74**:031306.
19. Abedi S, Rechenmacher AL, Faoro I. Vortex Structures inside Shear Bands in Sands. *Proceedings Geo-Frontiers 2011*, Dallas, TX, 13–16 Mar. 2011.
20. Walsh SDC, Tordesillias A, Peters JF. Development of micromechanical models for granular media. *Granular Matter* 2007; **9**(5):337–352.
21. Rechenmacher AL, Finno RJ. Digital Image Correlation to Evaluate Shear Banding in Dilative Sands. *Geotechnical Testing Journal* 2004; **27**(1):13–22.
22. Hall SA, Wood DM, Ibraim E, Viggiani G. Localised defolmation patterning in 2D granular materials revealed by digital image correlation. *Granular Matter* 2010; **12**(1):1–14.
23. Röchter L, Köning D, Schanz T, Triantafyllidis T. Shear banding and strain softening in plane strain extension: physical modeling. *Granular Matter* 2010; **12**(3):287–301.
24. Lesniewska D, Wood DM. Observations of Stresses and Strains in a Granular Material. *Journal of Engineering Mechanics* 2009; **135**(9):1038–1054.
25. Rechenmacher AL. Grain-scale processes governing shear band initiation and evolution in sands. *Journal of the Mechanics and Physics of Solids* 2006; **54**:22–45.
26. Chupin O, Rechenmacher A. Kinematics of Localized Shear in Granular Materials. *Proceedings 18th ASCE Engineering Mechanics Conference*, Blacksburg, VA, 3–6 June 2007.
27. Mooney MA. An experimental study of strain localization and the mechanical behavior of sand. *Ph.D. Thesis*, Northwestern University: Evanston, IL, 1996
28. Sutton MA, McNeill SR, Helm JD, Chao YJ. Advances in Two-Dimensional and Three-Dimensional Computer Vision. In *Photomechanics: Topics in Applied Physics*, Rastogi PK (ed.). Springer: Berlin, 2000; 323–372.
29. Sutton MA, Orteau J-J, Schreier HW. *Image Correlation for Shape, Motion and Deformation Measurements: Basic Concepts, Theory and Applications*. Springer: New York, 2009.
30. Chu TC, Ranson WF, Sutton MA, Peters WH. Applications of Digital-Image-Correlation Techniques to Experimental Mechanics. *Experimental Mechanics* 1985; **25**(3):232–245.
31. Sutton MA, Wolters WJ, Peters WH, Ranson WF, McNeil WR. Determination of Displacements Using an Improved Digital Correlation Method. *Image and Vision Computing* 1983; **1**(3):133–139.

32. Vendroux G, Knauss WG. Submicron deformaiton field measurements: Part 2. *Improved Digital Image Correlation. Experimental Mechanics* 1998; **38**(2):86–92.
33. Knauss WG, Chasiotis I, Huang Y. Mechanical measurements at the micron and nanometer scales. *Mechanics of Materials* 2003; **35**:217–231.
34. White DJ, Take WA, Bolton MD. Soil deformation measurement using particle image velocimetry and photogrammetry. *Geotechnique* 2003; **53**(7):619–631.
35. Schreier HW, Sutton MA. Systematic errors in digital image correlation due to undermatched subset shape functions. *Experimental Mechanics* 2002; **42**(3):303–310.
36. Gonzalez J, Knauss WG. Strain inhomogeneity and discontinuous drack growth in a particulate composite. *Journal of the Mechanics and Physics of Solids* 1998; **46**(10):1981–1995.
37. Bonet J, Wood RD. *Nonlinear Continuum Mechanics for Finite Element Analysis*. Cambridge University Press: Cambridge, 1997.
38. Rechenmacher AL, Abedi S. Length scales for nonaffine deformation in localized, granular shear. In *Proceedings of the 9th International Workshop on Bifurcation and Degradation in Geomaterials*, Bonelli S, Descalu C, Nicot F (eds.). Porquerolles, Provence, France, May 23–26 2011.